Flow Modulation by a Mushroom-Like Surface Coating in the Vicinity of a Wind-Turbine Airfoil Section

Ali Doosttalab,[1, a)] Suranga Dharmarathne,[2] Humberto Bocanegra Evans,[1] Ali M. Hamed,[3] Serdar Gorumlu,[1] Burak Aksak,[1] Leonardo P. Chamorro,[4] Murat Tutkun,[5, 6] and Luciano Castillo[2]

[1)] *Department of Mechanical Engineering, Texas Tech University, Lubbock, TX 79409, USA*

[2)] *School of Mechanical Engineering, Purdue University, West Lafayette, IN 47907, USA*

[3)] *Department of Mechanical Engineering, Union College, Schenectady, NY 12308, USA*

[4)] *Department of Mechanical Science and Engineering, University of Illinois, Urbana, IL 61801, USA*

[5)] *Department of Process and Fluid Flow Technology, Institute for Energy Technology (IFE), 2027 Kjeller, Norway*

[6)] *Department of Mathematics,University of Oslo, Blindern, 0316 Oslo, Norway*

(Dated: 26 April 2018)

The flow over a mushroom-shaped micro-scale coating was experimentally inspected over a diverging channel that followed the pressure side of a wind turbine blade (S835). High-resolution particle image velocimetry was used to obtain in-plane velocity measurements in a refractive-index-matching flume at Reynolds number $Re_\theta \approx 1200$ based on the momentum thickness. Results show that the evolution of the boundary layer thickness, displacement thickness, and shape factor change with the coating, contrary to the expected behavior of an adverse pressure gradient boundary layer over a canonical rough surface. Comparison of the flow with that over a smooth wall revealed that the turbulence production exhibited similar levels in both cases suggesting that the coating does not behave like a typical rough wall, which increases the Reynolds stresses. Proper orthogonal decomposition (POD) was used to decompose the velocity field to investigate the possible structural changes introduced by the wall region. It suggests that large-scale motions in the wall region lead to high-momentum flow over the coated case compared to the smooth counterpart. This unique behavior of this surface coating can be useful in wind-turbine applications, with great potential to increase the power production.

———
[a]ali.doosttalab@ttu.edu

I. INTRODUCTION

Flow separation plays a significant role in the drag experienced by terrestrial, marine, and aerial vehicles, among others.[1] A modest reduction of the separated flow generally leads to substantial energy savings. Flow separation occurs on wind turbine blades due to a large pressure gradient, which causes power losses and unsteady loading. The performance of wind turbines is sensitive to the surface characteristics of the blade surfaces. For instance, ice accretion increases the surface roughness and decreases lift-to-drag ratio;[2] the roughness induced by insect contamination, particularly at the leading edge, facilitates flow separation at normal operating conditions.[3] The phenomenon of 'double stall' is also attributed to the roughness effects created by insect contamination.[4] Similarly, deposition of dust or erosion due to sand blasting also results in performance reduction[5]. Overall, flow separation owing to natural causes should be mitigated to achieve designed performance of wind turbines.

Various studies have shown the distinctive role of surface roughness on flow separation. For instance, Song and Eaton[6] experimentally measured the separation bubble over a ramp expansion past a flat plate. Comparison of the flow over smooth and rough (sand-grain roughness) walls showed a significantly larger recirculation bubble in the latter. Cao and Tamura[7] carried out wind-tunnel experiments to quantify the effect of surface roughness on the turbulent boundary layer flow over a steep hill. They reported that surface roughness induced a larger separation bubble downstream of the hill as well as increased turbulence production. Torres-Nieves[8] investigated flow separation over a S809 airfoil experimentally and observed separation closer to the leading edge with sand-grain surface and a thicker boundary layer compared to the smooth case. Additionally, Zhang et al.[9] studied the role of leading edge pillars on low-Reynolds number airfoils and found that pillars of $250\,\mu m$ high at the leading edge delayed the stall angle of attack; whereas larger pillars of $500\,\mu m$ high, advanced the aerodynamic stall. Brzek et al.[10] studied adverse pressure-gradient (APG) flows over rough surfaces and reported a significant increase in skin friction and Reynolds stresses, even though the flow was not separated in that case. Freestream turbulence delays separation in smooth wind turbine blades;[11] however, the opposite effect occurs with rough blades.[8] Traditional passive flow control strategies such as riblets and vortex generators have been tested on wind turbines.[12,13]

The use of biologically-inspired coatings has attracted attention for drag reduction

purposes.[14,15] In particular, Dean and Bhushan[16], Büttner and Schulz[17] and Luo et al.[18] studied shark-skin inspired surfaces and observed drag reduction properties. Bixler and Bhushan[19] used shark-inspired riblets to reduce the skin friction drag in turbulent flows. Chamorro et al.[12] studied drag reduction in airfoils using triangular riblets and proposed an optimum design that achieved maximum total drag reduction. Lang et al.[20] investigated flow separation on APG flows over bio-inspired surfaces and discussed control mechanisms for separation. Direct numerical simulations of flow over shark skin-inspired denticles showed a significant drag increase.[21] They attributed this increase to the increase in the form drag due to the separated three-dimensional turbulent flow around the denticles. Using an array of $\vee$-shaped barriers, Sirovich and Karlsson[22] was able to obtain up to 12% skin friction drag reduction, and showed that the arrangement of the roughness structures is a leading factor in determining the changes in the drag.

Large-scale motions (LSMs) are organized structures in turbulent flows that have long correlation tails.[23] They have an approximate streamwise length scale of 2δ, where δ is the boundary layer thickness. LSMs are of great relevance in wind energy because they have been shown to carry more than 50% of the Reynolds stresses and kinetic energy in wall-bounded flows.[24,25] Those structures with streamwise length scales over 2δ, are referred as very large-scale motions (VLSMs).[26] Previous studies on canonical wall-bounded turbulent flows have confirmed the existence of LSMs and VLSMs both in laboratory[27,28] and field experiments.[29]

This study focuses on the boundary layer statistics of a separated flow over a bio-inspired surface coating (hereon referred as coated surface). The shape of the roughness elements are inspired by nature[30] and modeled as a mushroom-like structures. The ability of this specific surface to modify flow separation may help to improve the efficiency of wind turbines. Bocanegra Evans et al.[31] revealed that by using this specific micro-scale coating, the reverse flow area within the separation region is smaller. The mean velocity inflection point is moved downstream with the coating, manifesting a delay of separation. Both of these behaviors contradict the expectations from a typical rough surface.[6–8] Additionally, this surface coating falls in the hydraulically smooth regime,[32] yet it significantly modulates the inner and outer flow, i.e., the large scales of the separation bubble which manifest in the outer flow in a strong adverse pressure gradient flow.[31] By a set of experiments using particle image velocimetry (PIV) over the pressure side of a typical wind turbine airfoil

(S835) profile in a refractive-index-matching (RIM) flume, we seek to demonstrate that a small micro-scale surface coating with a roughness parameter of $k^+ = u_\tau k/\nu \sim 1.0$ (in the hydraulically smooth regime) leads to large scale flow modulations, contrary to the effects seen in typical surface roughness, where k is the roughness height, ν is the kinematic viscosity and u_τ ($= \sqrt{\tau_w/\rho}$, where τ_w is the wall shear stress, and ρ is the fluid density), is the friction velocity. These structures are roughly similar to the shape and the dimension of the denticles on the skin of the Mako shark (see figure 1). The selection of the pressure side of this airfoil ensured flow separation at the zero angle and smooth matching with the wall. We explore the changes on the separation bubble and the flow evolution induced by the coating, which directly affects the form drag. Another objective of this study is to examine how this bio-inspired micro-scale surface coating impacts flow separation in relation to LSMs and small scale motions (SSMs). Understanding how LSMs affect the flow physics on wind turbine blades could indeed help us design better flow control strategies that more effectively impact their performance by delaying or fully mitigating flow separation. The paper is organized as follows: §II describes the experimental setup; §III discusses the flow parameters and single point statistics and contrasts the LSMs and SSMs observed in both cases; and §IV summarizes the main observations.

II. EXPERIMENTAL SETUP

The separated flow over a bio-inspired coating was experimentally studied using a PIV system in a 2.5 m long RIM channel of 112.5 mm × 112.5 mm cross section at the University of Illinois. A diverging section was placed at the bottom wall of the channel to induce APG. This section followed a S835 foil profile within $0.249 < x_c/c < 0.945$, where c is the chord length, and x_c is the streamwise distance from the leading edge of the airfoil. The height of the flume within this region increased from $h_1 = 45$ mm to $h_2 = 112.5$ mm. The incoming flow developed over a length of $l/h_1 \approx 29$ before reaching the diverging region (figure 2a). The coordinate system $(x, y) = (0, 0)$ was set at the bottom wall, where the diverging section begins. Fine tune of the setup was inspected with an exploratory numerical simulation using Reynolds-Averaged Navier-Stokes (RANS) equations with a four equation SST-Transitional closure model[33] and second-order upwind discretization scheme. The purpose of such exploratory simulations were just to get a rough estimation of the
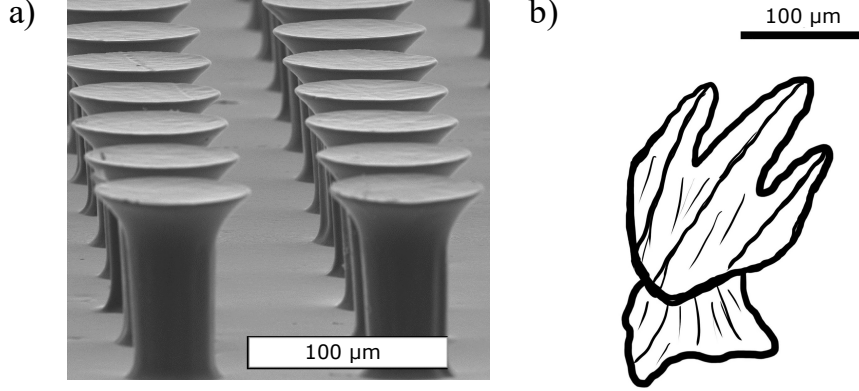
FIG. 1: Size and geometry comparison of micro-structures (in both a and b the bar represents 100 micron) a) micro-scale mushroom like structures considered in this study b) sketch of a shortfin mako (Isurus oxyrinchus) micro structure.

recirculation zone. This is illustrated in figure 3, which shows the mean streamwise velocity and streamlines over a smooth wall. The axis are normalized with δ_0, the boundary layer thickness before the expansion section, and the contours show the mean streamwise velocity.

The refractive index of the fluid (NaI aqueous solution, 63% by weight) is very similar to the material of the surface coating, which minimized reflection and allowed for measurements within the viscous sublayer ($y^+ \approx 3$). The NaI solution has a density $\rho = 1800\,\text{kg m}^{-3}$ and a kinematic viscosity $\nu \approx 1.1 \times 10^{-6}\,\text{m}^2\,\text{s}^{-1}$. The centerline velocity of the incoming flow, U_∞, was $\approx 0.225\text{m s}^{-1}$. The developed turbulent flow at the beginning of the APG region within the filed of view (FOV) 2 ($0.348 < x/c < 0.712$, where $c = 500\,\text{mm}$) had a Reynolds number based on momentum thickness of approximately 1200.

The coating consists of micro-scale pillars arranged in a square packing configuration. The pillars (as shown in figure 1a) have a cylindrical base and a diverging tip (see figure 2b). The stalk and tip diameters are $40\,\mu\text{m}$ and $75\,\mu\text{m}$, with a height of $85\,\mu\text{m}$ and a center-to-center separation of $120\,\mu\text{m}$ (≈ 1.5 wall units). With the given height, $85\,\mu\text{m}$ and $Re_\theta \approx 1200$, the roughness height parameter is $k^+ \approx 1$, which suggests a hydraulically smooth regime.[32] The fibers were manufactured from a rigid clear polyurethane (Crystal Clear 200, Smooth-On) via casting on a silicone rubber mold (Moldmax 27T, Smooth-On), which features the negative of the structures. Casting was performed with a $112.5\,\text{mm}$ by $500\,\text{mm}$ acrylic backing, and the polyurethane was observed to strongly adhere to it upon curing at room temperature for 72 hours. Details about the fabrication procedure for the micro-fibers can be found in

Aksak et al.[34] and Murphy et al.[35,36]. The micro-fibers were applied in the diverging wall within $x/c \in$ [-0.10, 0.90]; for reference, figure 2c depicts S835 airfoil, where the region in gray corresponds to the portion with coating in the diverging region.

A planar PIV system from TSI consisting of an 11 MP (4000 × 2672 pixels), 12 bit, frame-straddle, CCD camera and a 150 mJ/pulse, double pulsed laser (Quantel) was used to characterize two 180 mm × 120 mm flow fields, shown in figure 2a, as FOV1 and FOV2. The flow was seeded with $5\,\mu$m silver-coated, hollow glass spheres, and 4000 image pairs were collected at 1 Hz. The interrogation window had a size of 16×16 pixels and 50% overlap, resulting in the vector grid spacing of $365\,\mu$m. The comparison between the flow over the smooth and coated surfaces was performed with minimum differences in the incoming flow (at inlet of the expansion). Figure 2d shows that the mean velocity profiles of both smooth and coated surfaces at $x/c = 0$ are almost identical with pointwise differences under 1%. Furthermore, during the course of the PIV experiments, the particles seeded to the flow simulated a "dusty" environment. Results did not show accumulation of particles within the micro-scale structures.

III. RESULTS

A. Single-point statistics

Figure 4 illustrates an instant of the difference in the instantaneous streamwise velocity in the smooth and coated cases $(u_{coated} - u_{smooth})/U_\infty$, where u is the instantaneous streamwise velocity. The positive regions close to the wall show the increase in streamwise velocity over the coated surface compared with the smooth surface at the expansion. Due to the flow separation close to the wall, positive velocity difference is the result of stronger reverse flow regions experienced by the smooth surface compared with the coated surface. However, away from the wall, the coated and smooth surfaces have nearly the same velocity, as evidenced in figure 4. In contrast with the coated case, the reverse flow regions are observed over large areas close to the wall for the smooth surface.[31]

A profile of the mean streamwise velocity, U, at an arbitrary location within this region ($x/c \approx 0.570$, which corresponds to the separation region where $Re_\theta \approx 1238$ and 1277 for the smooth and coated cases, respectively) is shown in figure 5a. The close look near the
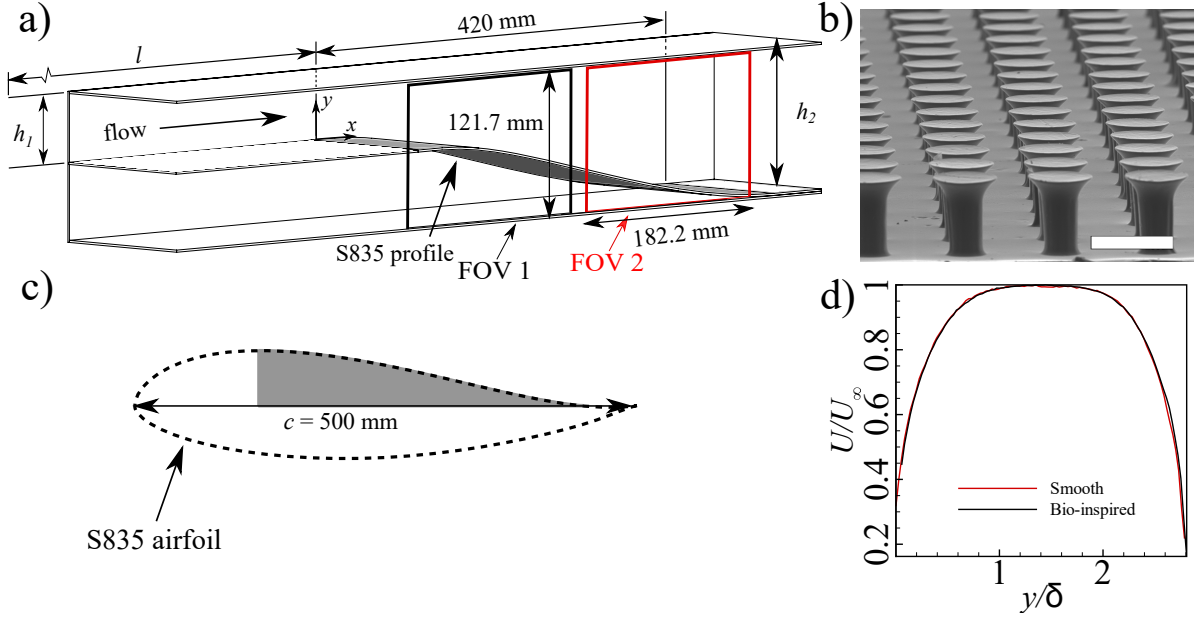
FIG. 2: a) Schematic of the flume; b) SEM image of the micro-pillar array; scale bar: $100\,\mu$m. c) vertically flipped S835 airfoil and the section used for the experiments; d) mean streamwise velocity at the inlet ($x/c = 0$).
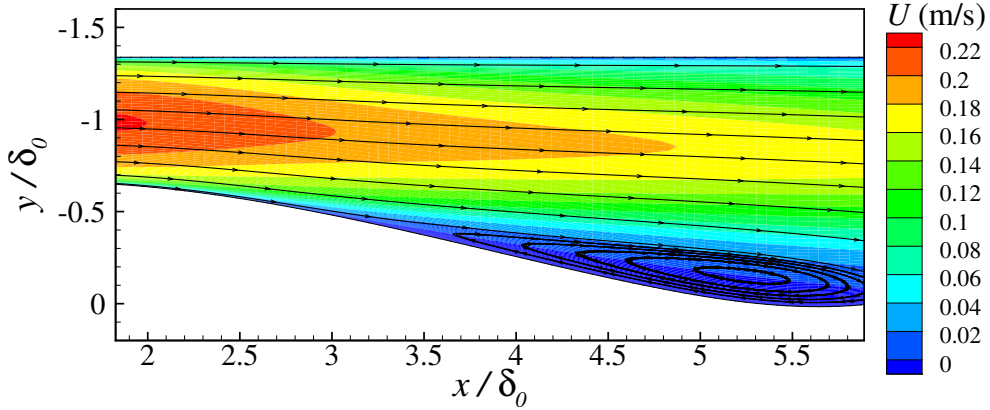

FIG. 3: Section of the smooth wall domain with contours of streamwise velocity and streamlines from the preliminary RANS simulations.

wall illustrated in figure 5b, reveal a larger negative region with the smooth wall. There, the velocity and vertical coordinate are normalized by U_∞ and δ. Here, the coated surface reduces the reverse flow, induces higher velocity over the inner region and part of the outer flow. This also suggests a reduction in the size of the recirculation bubble, as shown by Bocanegra Evans et al.[31]. Figure 6a shows the normalized vertical velocity V/U_∞ at the
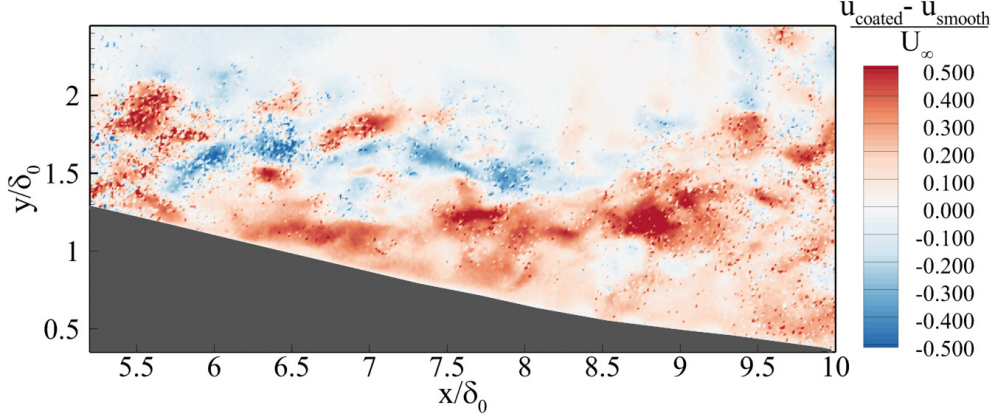
FIG. 4: Instantaneous streamwise velocity difference between the smooth and coated cases.

same location. Close to the wall (shown in figure 6b), the positive V/U_∞ is associated with the upward motion of the flow in the separation region. The increased V/U_∞ (toward the wall) over the coated surface, further supports the reduction in the size of the separation bubble deduced from the higher streamwise velocity in the inner region of the flow. Similar results were obtained at other streamwise locations in the separation region (not shown here for brevity). It is important to stress that such flow modulation is induced by a surface roughness, which is considered hydraulically smooth. This indicates that not only the height plays a role on flow modification, but also the topographical features, i.e. the shape and arrangement of the roughness elements, as compared to similar studies using randomly staggered sandpaper roughness.[6,31] Sirovich and Karlsson[22] showed that aligned ∨-shaped roughness elements caused drag increase, while random arrangement reduced it. However, their roughness elements were considerably larger ($k^+ \approx 5-6$), which points out a different physical mechanism.

The Reynolds number based on the boundary layer thickness, Re_δ ($= U_\infty\delta/\nu$), as a function of the Reynolds number Re_x ($= U_\infty x/\nu$) is shown in figure 7a. Re_δ is consistently lower in the coated case, suggesting a reduction in the recirculation bubble as pointed by Bocanegra Evans et al.[31]. This result reveal a non-standard behavior of APG flow over canonical rough surfaces presented in literature[6,37], where turbulent diffusion induced by the surface roughness produces a thicker boundary layer. Also, the evolution of the displacement thickness, δ^* (equation 1) in terms of the associated Reynolds number Re_{δ^*} ($= U_\infty(x)\delta^*/\nu$),
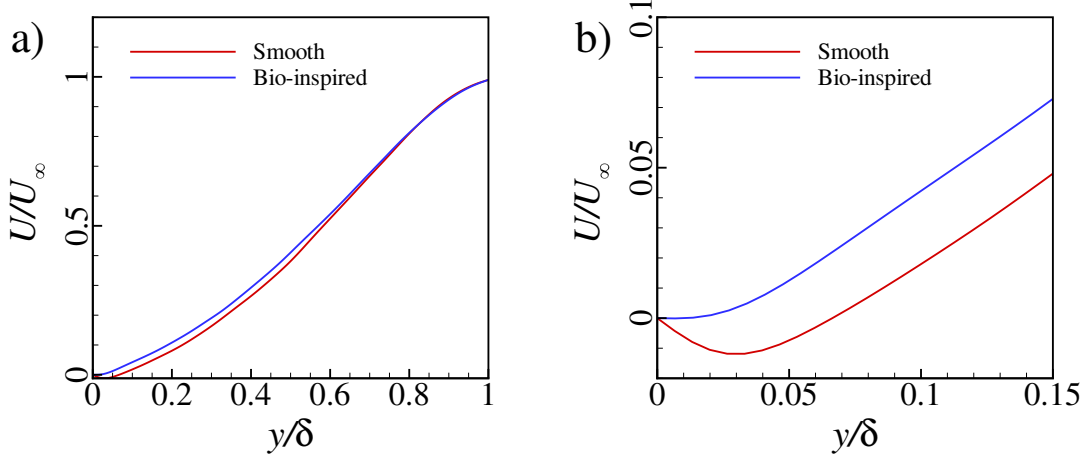
FIG. 5: a) Mean normalized streamwise velocity (U/U_∞) profiles within the separated region at $x/c \approx 0.57$; b) close to the wall.
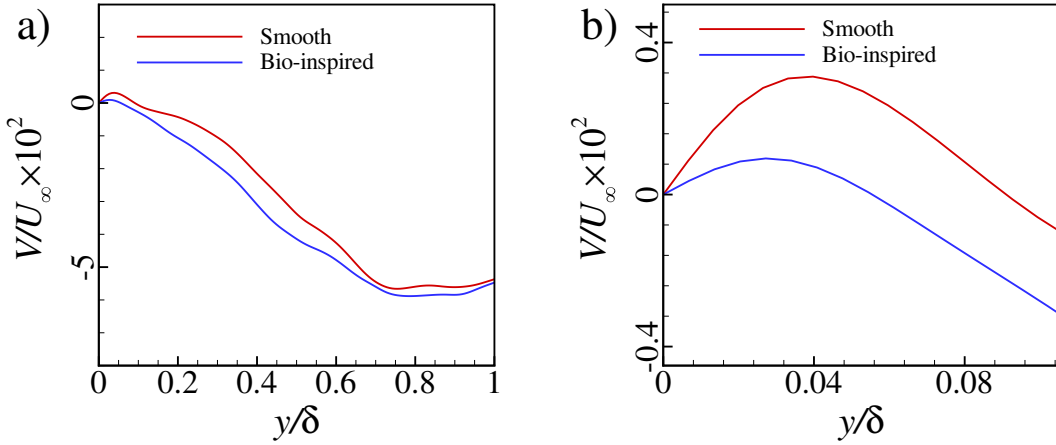

FIG. 6: a) Mean normalized vertical velocity (V/U_∞) profiles within the separated region at $x/c \approx 0.57$; b) close to the wall.

is shown in figure 7b, where

$$\delta^* = \int_0^\delta (1 - \frac{U}{U_\infty})dy. \tag{1}$$

Note that Re_{δ^*} is also lower with the coating, where the peak at $Re_x \approx 50000$ is reduced about 7%; again, this behavior does not follow classic flow over canonical rough walls. The shape factor, $H = \delta^*/\theta$, is illustrated in figure 7c. This quantity monotonically increases with distance in APG flows with separation.[38] However, it is significantly lower with the coating (10% maximum reduction) implying that the flow has a lower tendency to separate. A sharp reduction in H, which is attributed to flow re-attachment, can be observed for both
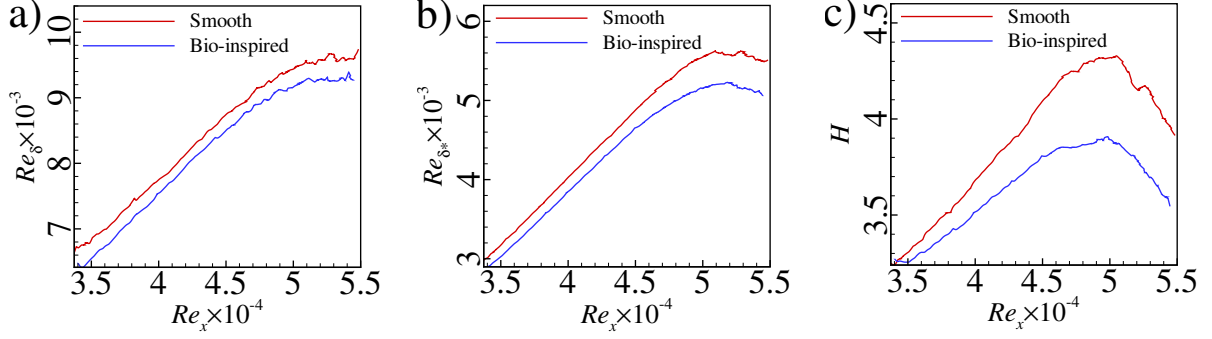
FIG. 7: Streamwise variation of Reynolds number based on a) boundary layer thickness, and b) displacement thickness for the smooth and coated cases; c) shape factor.

cases at $Re_x \approx 5 \times 10^4$.

Conventional rough surfaces are usually associated with increased turbulent kinetic energy production and higher Reynolds stresses;[37,39] however, this is not the case with the present coating, since the flow is in the hydrodynamically smooth regime.[32] Figures 8a,b show the $\overline{u'u'}$ and $\overline{v'v'}$ components of the Reynolds normal stresses; here, the overbar represents ensemble averaging. Interestingly, the $\overline{v'v'}$ component in the outer region is also modulated by the coating, without dampening the viscous sub-layer, which typically occurs in sand-grain surface roughness. This phenomenon observed in the present study and the sand-grain roughness experiments from Torres-Nieves[8] motivates examining Townsend's hypothesis[40] for rough APG flows. It states that at sufficiently high Re and at a distance of few roughness heights away from the wall, turbulence statistics in the outer flow should be independent of the surface. Jiménez[39] introduced another condition which states that, k/δ should be smaller than 0.02 for Townsend's hypothesis to be valid. As presented earlier, the equivalent roughness parameter of the coating is still in the hydraulically smooth regime, and is not sufficiently large to induce roughness effects which can penetrate into the outer flow. One should also note that the Re in the present study is moderate, which potentially, partially satisfies the sufficiently high Reynolds number assumption made in the original hypothesis by Townsend. However, with these two conditions (i.e. small enough roughness and moderate Re) satisfied, the modifications on the flow are confined to the roughness sublayer ($< 5k$) which was confirmed by Doosttalab et al.[41] using single point statistics over an irregular surface roughness in a zero-pressure-gradient boundary layer. Even though the first condition is partially satisfied for the surface coating in the present study, the flow modulation in the
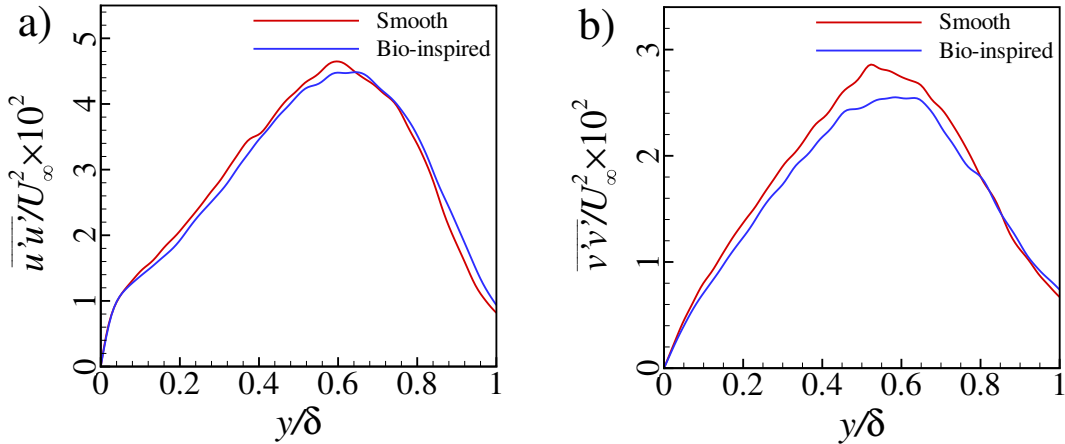
11

FIG. 8: Reynolds normal stresses a) $\overline{u'u'}$ and b) $\overline{v'v'}$ for the smooth and coated surfaces.

outer region of the boundary layer is significant – especially since it modulates the separation bubble.

Figure 9a shows a comparison of the Reynolds shear stress $\overline{u'v'}$. This quantity typically increases with rough walls, as seen in Brzek et al.[10] (due to turbulence diffusion in the wall region); however, the coating does not induce change; this may be attributed to the reduced height of the pillars (hydrodynamically smooth surface). Figure 9b illustrates the turbulence kinetic energy (TKE) production, P, considering the dominating terms, as follows:

$$P = -\overline{u'v'}\frac{dU}{dy} - \overline{v'v'}\frac{dV}{dy}. \tag{2}$$

This quantity is very similar in both cases, and shows a slight decrease in the peak of production for the coated surface. The change in TKE is critical for drag reduction, given that it increases viscous drag.[39] If the form drag is reduced, due to the reduction in the separation bubble, and P is maintained, the coating may be capable of reducing the total drag. Compared to the Song and Eaton[6], where an increase of P was observed over a rough surface, we can conclude that this surface coating is not a rough surface.

While the mechanism responsible for the modification of the flow is not entirely clear, experiments by Bocanegra Evans et al.[42] shed light on the flow around pillars with simplified configuration. There, regions of high and low pressure were observed within a canopy of cylindrical micro-pillars, even at very low velocities, as illustrated in figure 10. The pressure fluctuations generate ejections (blowing) and sweeps (suction), which in turn modify the interaction between the flow and the wall. As a result, the separation bubble is reduced and
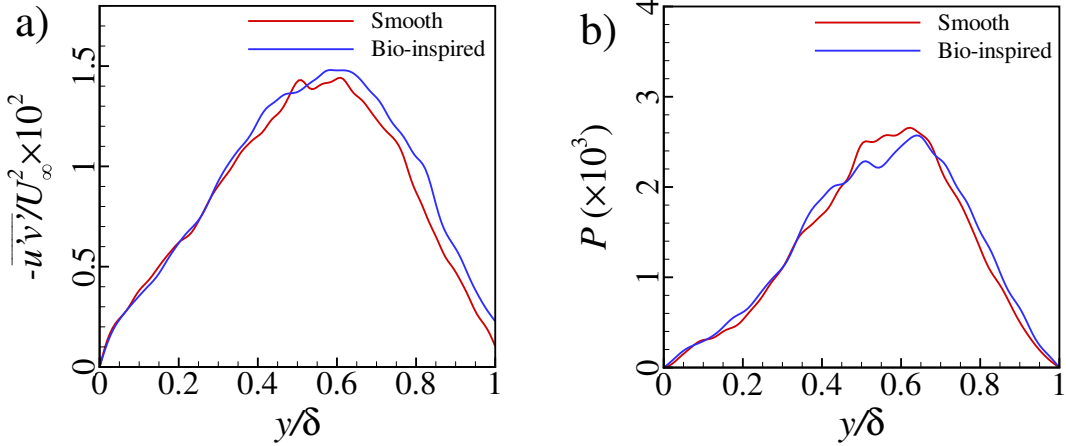
FIG. 9: a) Reynolds shear stress $\overline{u'v'}$; b) turbulence kinetic energy production P for the smooth and coated surfaces.

the near-wall velocity is increased as observed in figures 4a, 4b, 5b,6b. This result contrasts with typical rough surfaces, where the near-wall region is dominated by increased turbulence and viscous diffusion, which leads to a thicker boundary layer and higher drag.

B. Shape Factor and Separation Criterion

Castillo et al.[38] employed the Von Kármán integral equation and the similarity pressure parameter Λ_θ with the wall shear stress to derive a formulation for the skin friction coefficient,

$$\frac{C_f}{2} = \frac{d\theta}{dx} \left\{ 1 - (2 + H)\Lambda_\theta \right\}, \tag{3}$$

where Λ_θ is the pressure parameter defined as,[38]

$$\Lambda_\theta \equiv \frac{\theta}{\rho U_\infty^2 d\theta/dx} \frac{dP_\infty}{dx} = -\frac{\theta}{U_\infty d\theta/dx} \frac{dU_\infty}{dx} = constant. \tag{4}$$

H can be related with the pressure parameter 'if equilibrium exists', and considering that $C_f \to 0$ at the separation, then H_{sep} is given only by the similarity pressure parameter,

$$H_{sep} = -\left[2 - \frac{1}{\Lambda_\theta} \right]. \tag{5}$$

The calculated values for pressure parameters Λ_θ, Λ_δ and $\Lambda_{\delta*}$ are shown and compared to literature[38] in table I, where Λ_δ and $\Lambda_{\delta*}$ are defined based on δ and δ^* as length scale instead of θ in equation 4. Figure 11 shows H as a function of δ^*/δ for the smooth (red) and coated
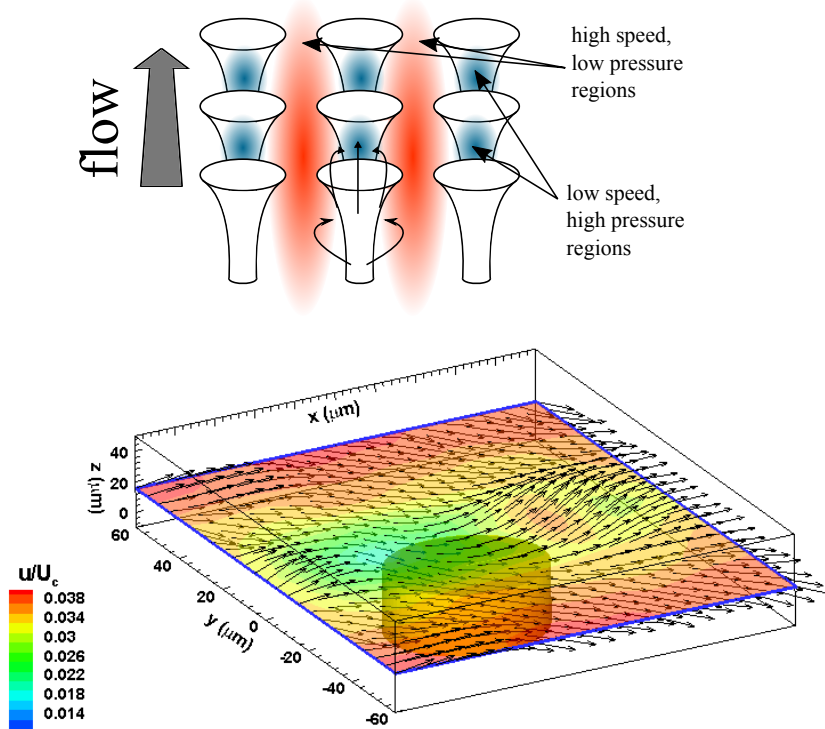
FIG. 10: Schematic of the possible physical mechanism. Red and blue colors in the upper figure indicate high speed - low pressure and low speed - high pressure zones, which by generating ejections and sweeps due to pressure differences, modify the fluid and the wall interactions as shown in the bottom figure. Adapted from Bocanegra Evans et al. [42] (CC-BY 4.0 license).

(black) with values from Castillo et al. [38]. The current data follows the general trend given by the experimental results from Simpson et al. [43,44], Alving and Fernholz [45]. This suggests that a correlation exists between H and δ^*/δ in both smooth and coated cases, even in separated flows. Note that this data is located in the outer limits of the intermittently separated and within the fully separated region. Furthermore, the flow over the coated surface has lower H (about 10% reduction in the peak value), which corresponds to a lower tendency for separation. The sharp fall of the current data is attributed to flow reattachment.

C.   Effect of surface coating on large-scale motions.

This section demonstrates the influence of the surface coating on the LSMs of the flow. To identify different scales, the flow needs to be decomposed into its constituent scales. This
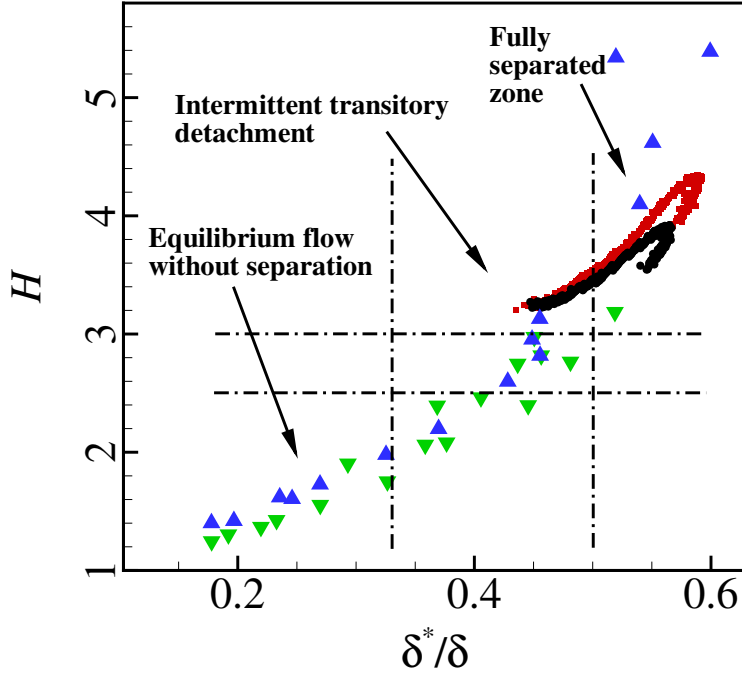
FIG. 11: H vs δ^*/δ for APG flows with separation for the smooth and coated surfaces. ▲
– experimental data of Simpson et al.[43,44]; ▼ – experimental data of Alving and
Fernholz[45]; ■ – smooth case; ● – coated case.

	Λ_δ	Λ_θ	$\Lambda_{\delta*}$
Castillo et al.[38]	0.23 ± 0.02	0.21 ± 0.01	0.19 ± 0.03
Smooth	0.23	0.27	0.16
Coating	0.25	0.25	0.17

TABLE I: Pressure parameters for the smooth and coated surfaces.

study uses the snapshot method[46] of proper orthogonal decomposition (POD) to separate the flow into its components. POD identifies different scales of the flow by eigenfunctions or eigenmodes (or simply modes) based on an ensemble of fluctuating velocity fields, $\{\boldsymbol{u}(x, y, t_k)\}_{k=1}^{N_t}$, where k and N_t represent sample number and total number of samples, respectively. In this study, $N_t = 4000$. The eigenfunctions are ordered according to their turbulence kinetic energy content and denoted by $\boldsymbol{\phi}^m(x, y)$, where m is the mode number. The amount of turbulence kinetic energy of the mth eigenmode (or scale), is given by

the corresponding eigenvalue, λ^m. Snapshot method decomposes the velocity field into N_t number of eigenmodes (or scales). Therefore, the velocity field of the kth sample can be reconstructed according to,

$$\boldsymbol{u}(x, y, t_k) = \sum_{m=1}^{N_t} b^m(t_k)\boldsymbol{\phi}^m(x, y), \tag{6}$$

where $b^m(t_k)$ is the coefficient that represents m^{th} mode and the kth sample. Using the linear property of the POD reconstruction, we can now divide the flow field into two groups as shown in equation (7): large-scale motions and small-scale motions.

$$\boldsymbol{u}(x, y, t_k) = \underbrace{\sum_{m=1}^{M_c} b^m(t_k)\boldsymbol{\phi}^m(x, y)}_{LSM} + \underbrace{\sum_{m=M_c+1}^{N_t} b^m(t_k)\boldsymbol{\phi}^m(x, y)}_{SSM}, \tag{7}$$

where M_c is the cut-off mode number. To find M_c such that the LSM field contains the physically realizable large-scales of the flow, we compared the logitudinal auto-correlation function, ρ_{uu}, of the LSM field with that of the original velocity field by gradually increasing the value of M_c. The flow over the smooth surface was chosen as the baseline case to determine M_c. In this case, when $M_c = 532$, auto-correlation functions of the LSM field and the original field becomes zero (i.e., $\rho_{uu} = 0$) approximately the same distance from the reference location, $\delta x/\delta_0 = 0$. Figure 12 shows ρ_{uu} of the LSM field (solid red) and that of the original field (solid black). According to the figure, both curves reach $\rho_{uu} = 0$ when $\delta x \approx 1.8\delta_0$. We can also observe that the pointwise difference between two auto-correlation functions is negligibly small. The close correspondence between two auto-correlation functions confirms that the LSM field contains physically realizable largest scales of the flow when $M_c = 532$.

Now, it is required to find the cut-off mode number for the coated case. The cut-off mode number for the coated case is obtained such that the LSM field of the coated case contains the same amount of energy of that of the smooth case. In figure 13, the fraction of energy recovered, χ_M, by M number of modes for the smooth (solid blue) and coated (solid red) cases is shown. The fraction of energy recovery is defined by

$$\chi_M = \frac{\sum_{m=1}^{M} \lambda^m}{\sum_{m=1}^{N_t} \lambda^m}. \tag{8}$$

The figure shows that $M_c = 532$ for the smooth case corresponds to 65% of turbulence kinetic energy suggesting that merely 13% of modes represents the largest scales of the flow,
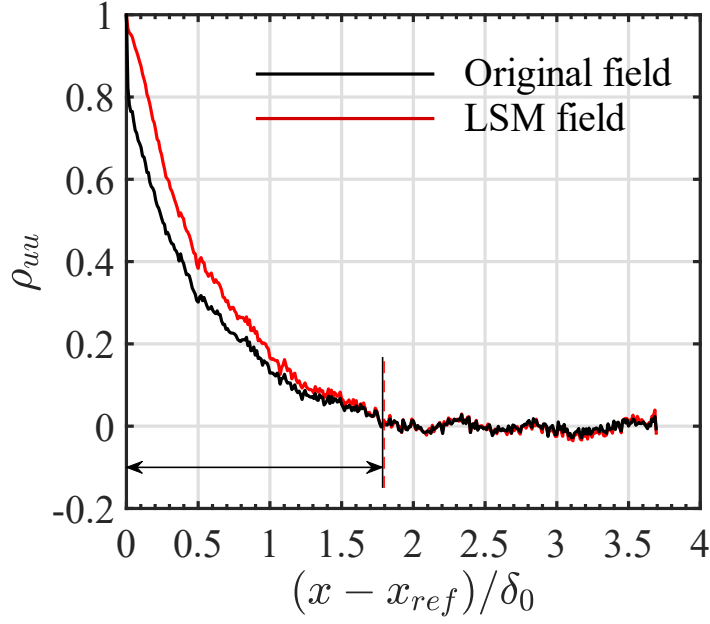
16

FIG. 12: Auto-correlation function of the streamwise velocity fluctuations. Solid black, ρ_{uu} for the original field; solid red, ρ_{uu} for the LSM field of the smooth case.
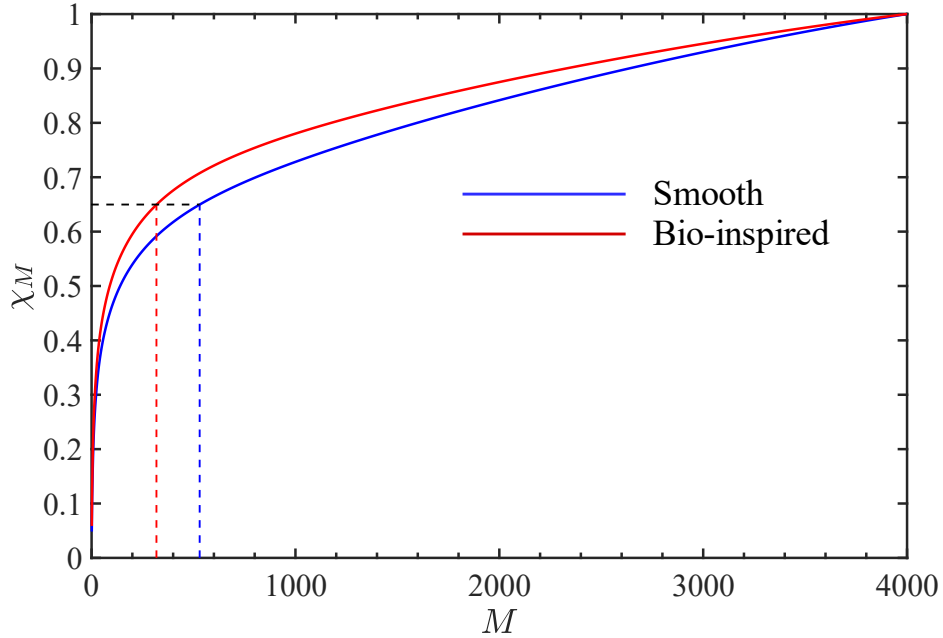

FIG. 13: The fraction of energy recovered by M number of modes. Solid red, coated; solid blue, smooth. Dashed blue and dashed red lines indicate the number of modes required to capture 65% of energy for the smooth and the coated case, respectively.
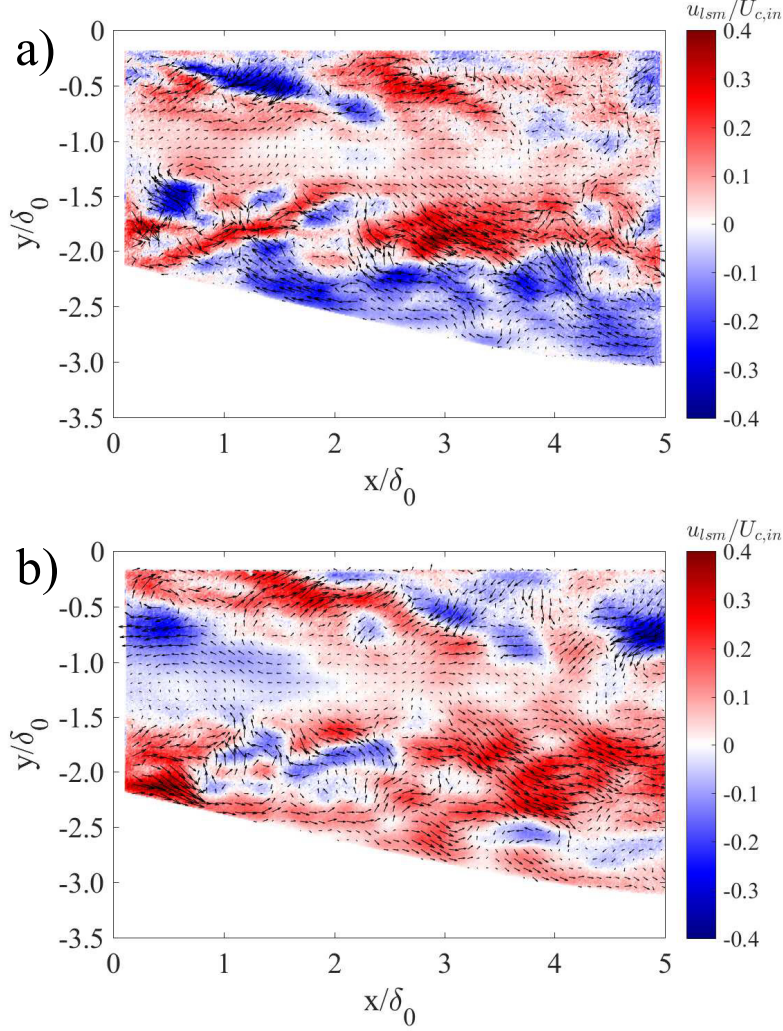
FIG. 14: Color contours represent the large-scale motion component of the instantaneous streamwise velocity fluctuations normalized by the mean centerline velocity at the inlet $(u_{lsm}/U_{c,in})$. Arrows indicate the instantaneous velocity vector field of large-scale motions $(u_{lsm}/U_{c,in}, v_{lsm}/U_{c,in})$ for (a) the smooth wall and (b) the coated wall.

which contain 65% of the energy. According to the figure, the number of mode required for the coated case to capture an equivalent amount of energy is 320. This indicates that the coating has increased the energy of large-scale motions. By using the cut-off mode of each case, we can obtain the LSMs fields for the smooth and coated cases according to

$$\boldsymbol{u}_{lsm}(x, y, t_k) = \sum_{m=1}^{532} b^m(t_k)\boldsymbol{\phi}^m(x, y) \tag{9}$$

18

and

$$\boldsymbol{u}_{lsm}(x, y, t_k) = \sum_{m=1}^{320} b^m(t_k)\boldsymbol{\phi}^m(x, y), \tag{10}$$

respectively. To observe how the LSMs in both cases look like, the LSM velocity fields are shown in figure 14. Over the smooth wall, a large-scale low-speed motion dominates the flow near the bottom wall (see figure 14a). The instantaneous velocity vector field (arrows) indicates that the flow is dominated by ejections. The reversed flow might be a consequence of the flow separation observed at the trailing edge of the airfoil. Figure 14b shows that a long high-speed region dominates the flow over the coated surface. The arrows show that the instantaneous flow is predominantly towards the direction of the mean flow near the bottom wall and that the sweeps dominate the near-wall region. Alternating high- and low-speed patterns of large-scale features near the top wall can be observed, where the wall is smooth and boundary layer is not separated. This observations sufficiently explain that the coating modifies the large-scale motions of the flow, specifically near the wall region, causing higher streamwise velocity near the wall, as shown earlier in figure 4.

IV. CONCLUSION

The coating led to a reduction of the reverse flow and higher streamwise and vertical velocities over most of the inner region and portion of the outer flow, which resulted in a reduction of the separation bubble. The most salient result is that a hydraulically smooth surface coating, with $k^+ \sim 1$ leads to global flow modulations, especially of the separation bubble, contrary to what is expected with a hydraulically smooth surface and of typical surface roughness.

Distributions of the Reynolds stresses and turbulence production indicate that the coating does not produce additional turbulence as typically observed in rough surfaces. It does not behave as a typical roughness, but induces macro-scale changes in the flow, i.e., it modulates the inner and outer regions of the flow. The physical mechanism induced by the coating is believed to be related with pressure modulation at the wall induced by the flow field around the micro-structures, thus locally producing regions of strong suction and blowing. This suggests that in addition to the height of the roughness elements, the topography plays an influential role in drag reduction on the wind turbine section.

POD analysis revealed that the flow over the coated surface contains more energetic

scales, represented by larger scale features associated with high momentum. This difference can be attributed to the different topographical characteristics of the bio-inspired roughness presented in this study with respect to standard sand-grain roughness. The fact that the coating mitigates the separation bubble and works under wetted conditions, as opposed to super-hydrophobic surfaces, opens possibilities for a wide range of applications besides wind energy. Mitigation of separation bubble will result in higher lift to drag ratio for airfoils used in wind turbines as the separation is a big issue here. Both horizontal and vertical axis wind turbines may benefit from this surface coating due to reduction of flow separation. For horizontal axis turbines, potential gains, include enhanced lift, as well as reduced acoustic noise and mechanical vibration. When the vertical axis turbines are considered, the positive impact is largely on higher generation of lift due to improved performance at high angles of attack. Due to structural considerations, thick airfoils are used in the root section of wind turbine blades, which are prone to flow separation. By using coated surfaces with this kind of flow control properties, the efficiency of the energy conversion might be improved while reducing the vortex shedding that negatively impacts the structural integrity of the turbine and the generation of noise.

ACKNOWLEDGMENTS

REFERENCES

[1] Y. Na and P. Moin. Direct numerical simulation of a separated turbulent boundary layer. *J. Fluid Mech.*, 374:379–405, 1998.

[2] C. Hochart, G. Fortin, J. Perron, and A. Ilinca. Wind turbine performance under icing conditions. *Wind Energy*, 11(4):319–333, 2008. ISSN 1099-1824. doi:10.1002/we.258. URL `http://dx.doi.org/10.1002/we.258`.

[3]G. P. Corten and H. F. Veldkamp. Aerodynamics: Insects can halve wind-turbine power. *Nature*, 412(6842):41–42, 2001.

[4]G. P. Corten and H. F. Veldkamp. *Insects cause double stall*. Netherlands Energy Research Foundation, 2001.

[5]N Dalili, A Edrisy, and R Carriveau. A review of surface engineering issues critical to wind turbine performance. *Renew. Sustainable Energy Rev.*, 13(2):428–438, 2009.

[6]S. Song and J. Eaton. The effects of wall roughness on the separated flow over a smoothly contoured ramp. *Exp. Fluids*, 33(1):38–46, 2002. ISSN 1432-1114. doi:10.1007/s00348-002-0411-1. URL http://dx.doi.org/10.1007/s00348-002-0411-1.

[7]S. Cao and T. Tamura. Experimental study on roughness effects on turbulent boundary layer flow over a two-dimensional steep hill. *J. Wind Eng. Ind. Aerodyn.*, 94(1):1 – 19, 2006. ISSN 0167-6105. doi:http://dx.doi.org/10.1016/j.jweia.2005.10.001. URL http://www.sciencedirect.com/science/article/pii/S0167610505001108.

[8]S. N. Torres-Nieves. *Interaction of turbulent length scales with wind turbine blades*. PhD thesis, Rensselaer Polytechnic Institute, 2011.

[9]Y. Zhang, T. Igarashi, and H. Hu. Experimental investigations on the performance degradation of a low-Reynolds-number airfoil with distributed leading edge roughness. In *49th AIAA Aerospace Sciences Meeting including the New Horizons Forum and Aerospace Exposition*, page 1102, 2011.

[10]B. Brzek, D. Chao, Ö. Turan, and L. Castillo. Characterizing developing adverse pressure gradient flows subject to surface roughness. *Exp. Fluids*, 48(4):663–677, 2010. ISSN 1432-1114. doi:10.1007/s00348-009-0759-6. URL http://dx.doi.org/10.1007/s00348-009-0759-6.

[11]V. Maldonado, L. Castillo, A. Thormann, and C. Meneveau. The role of free stream turbulence with large integral scale on the aerodynamic performance of an experimental low Reynolds number s809 wind turbine blade. *J. Wind Eng. Ind. Aerodyn.*, 142:246–257, 2015.

[12]L. P. Chamorro, R.E.A. Arndt, and F. Sotiropoulos. Drag reduction of large wind turbine blades through riblets: Evaluation of riblet geometry and application strategies. *Renew. Energ.*, 50:1095 – 1105, 2013. ISSN 0960-1481. doi:http://dx.doi.org/10.1016/j.renene.2012.09.001. URL http://www.sciencedirect.com/science/article/pii/S0960148112005630.

[13]WA Timmer and RPJOM Van Rooij. Summary of the delft university wind turbine dedicated airfoils. In *ASME 2003 Wind Energy Symposium*, pages 11–21. American Society of Mechanical Engineers, 2003.

[14]G. V. Lauder, D. K. Wainwright, A. G. Domel, J. C. Weaver, L. Wen, and K. Bertoldi. Structure, biomimetics, and fluid dynamics of fish skin surfaces*. *Phys. Rev. Fluids*, 1: 060502, Oct 2016. doi:10.1103/PhysRevFluids.1.060502. URL `http://link.aps.org/doi/10.1103/PhysRevFluids.1.060502`.

[15]Dennis M Bushnell and KJ Moore. Drag reduction in nature. *Annu. Rev. Fluid Mech.*, 23 (1):65–79, 1991.

[16]B. Dean and B. Bhushan. Shark-skin surfaces for fluid-drag reduction in turbulent flow: a review. *Phil. Trans. R. Soc. A*, 368(1929):4775–4806, 2010. ISSN 1364-503X. doi:10.1098/rsta.2010.0201. URL `http://rsta.royalsocietypublishing.org/content/368/1929/4775`.

[17]C. C. Büttner and U. Schulz. Shark skin inspired riblet structures as aerodynamically optimized high temperature coatings for blades of aeroengines. *Smart Mater. Struct.*, 20 (9):094016, 2011. URL `http://stacks.iop.org/0964-1726/20/i=9/a=094016`.

[18]Y. H. Luo, X. Li, D. Y. Zhang, and Y. F. Liu. Drag reducing surface fabrication with deformed sharkskin morphology. *Surf. Eng.*, 32(2):157–163, 2016. doi:10.1179/1743294415Y.0000000037.

[19]G. D. Bixler and B. Bhushan. Fluid drag reduction with shark-skin riblet inspired microstructured surfaces. *Adv. Funct. Mater.*, 23(36):4507–4528, 2013. ISSN 1616-3028. doi:10.1002/adfm.201203683. URL `http://dx.doi.org/10.1002/adfm.201203683`.

[20]A. Lang, P. Motta, M. L. Habegger, R. Hueter, and F. Afroz. Shark skin separation control mechanisms. *Mar. Technol. Soc. J.*, 45(4):208–215, 2011. ISSN 0025-3324. doi: doi:10.4031/MTSJ.45.4.12.

[21]A. Boomsma and F. Sotiropoulos. Direct numerical simulation of sharkskin denticles in turbulent channel flow. *Phys. Fluids*, 28(3):035106, 2016. doi: http://dx.doi.org/10.1063/1.4942474. URL `http://scitation.aip.org/content/aip/journal/pof2/28/3/10.1063/1.4942474`.

[22]L. Sirovich and S. Karlsson. Turbulent drag reduction by passive mechanisms. *Nature*, 388(6644):753–755, 1997.

[23]K. C. Kim and R. J. Adrian. Very large-scale motion in the outer layer. *Phys. Fluids*,

11(2):417–422, 1999. doi:http://dx.doi.org/10.1063/1.869889. URL `http://scitation.aip.org/content/aip/journal/pof2/11/2/10.1063/1.869889`.

[24] B.J Balakumar and R.J Adrian. Large- and very-large-scale motions in channel and boundary-layer flows. *Phil. Trans. R. Soc. A*, 365(1852):665–681, 2007. ISSN 1364-503X. doi:10.1098/rsta.2006.1940.

[25] Z. Liu, R. J. Adrian, and T. J. Hanratty. Large-scale modes of turbulent channel flow: transport and structure. *J. Fluid Mech.*, 448:53–80, 12 2001. ISSN 1469-7645. doi:10.1017/S0022112001005808. URL `http://journals.cambridge.org/article_S0022112001005808`.

[26] M. Guala, S. E. Hommema, and R. J. Adrian. Large-scale and very-large-scale motions in turbulent pipe flow. *J. Fluid Mech.*, 554:521–542, 5 2006. ISSN 1469-7645. doi:10.1017/S0022112006008871. URL `http://journals.cambridge.org/article_S0022112006008871`.

[27] N. Hutchins and I. Marusic. Evidence of very long meandering features in the logarithmic region of turbulent boundary layers. *J. Fluid Mech.*, 579:1–28, 5 2007b. ISSN 1469-7645. doi:10.1017/S0022112006003946. URL `http://journals.cambridge.org/article_S0022112006003946`.

[28] M. Tutkun, W. K. George, J Delville, M Stanislas, PBV Johansson, J-M Foucaut, and S. Coudert. Two-point correlations in high Reynolds number flat plate turbulent boundary layers. *J. Turbul.*, (10):N21, 2009.

[29] N. Hutchins, K. Chauhan, I. Marusic, J. Monty, and J. Klewicki. Towards reconciling the large-scale structure of turbulent boundary layers in the atmosphere and laboratory. *Bound.-Layer Meteorol.*, 145(2):273–306, 2012. ISSN 1573-1472. doi:10.1007/s10546-012-9735-4. URL `http://dx.doi.org/10.1007/s10546-012-9735-4`.

[30] G. S. Watson, D. W. Green, L. Schwarzkopf, X. Li, B. W. Cribb, S. Myhra, and J. A. Watson. A gecko skin micro/nano structure a low adhesion, superhydrophobic, antiwetting, self-cleaning, biocompatible, antibacterial surface. *Acta Biomater.*, 21:109 – 122, 2015. ISSN 1742-7061. doi:http://dx.doi.org/10.1016/j.actbio.2015.03.007. URL `http://www.sciencedirect.com/science/article/pii/S1742706115001075`.

[31] H. Bocanegra Evans, A. M. Hamed, S. Gorumlu, A. Doosttalab, B. Aksak, L. P. Chamorro, and L. Castillo. Engineered bio-inspired coating for passive flow control. 2017. doi:10.1073/pnas.1715567115. In press Proc. Natl. Acad. Sci. U.S.A.

[32] H. Schlichting. In *Boundary-layer theory*. McGraw-Hill, 1968.

[33] R. Langtry and F. Menter. Transition modeling for general CFD applications in aeronautics. In *43rd AIAA Aerospace Sciences Meeting and Exhibit*, page 522, 2005.

[34] B. Aksak, M. P. Murphy, and M. Sitti. Adhesion of biologically inspired vertical and angled polymer microfiber arrays. *Langmuir*, 23(6):3322–3332, 2007. doi:10.1021/la062697t. PMID: 17284057.

[35] M. P. Murphy, B. Aksak, and M. Sitti. Adhesion and anisotropic friction enhancements of angled heterogeneous micro-fiber arrays with spherical and spatula tips. *J. Adhes. Sci. Technol.*, 21(12-13):1281–1296, 2007.

[36] M. P. Murphy, B. Aksak, and M. Sitti. Gecko-inspired directional and controllable adhesion. *Small*, 5(2):170–175, 2009.

[37] B. Brzek, R. B. Cal, G. Johansson, and L. Castillo. Inner and outer scalings in rough surface zero pressure gradient turbulent boundary layers. *Phys. Fluids*, 19(6):065101, 2007. doi:http://dx.doi.org/10.1063/1.2732439. URL `http://scitation.aip.org/content/aip/journal/pof2/19/6/10.1063/1.2732439; jsessionid=P69xdMzkURLk-L4JeZJgzBzz.x-aip-live-03`.

[38] L. Castillo, X. Wang, and W. K. George. Separation criterion for turbulent boundary layers via similarity analysis. *J. Fluids Eng.*, 126(3):297–304, 2004.

[39] J. Jiménez. Turbulent flows over rough walls. *Annu. Rev. Fluid Mech.*, 36(1):173–196, 2004. doi:10.1146/annurev.fluid.36.050802.122103. URL `http://dx.doi.org/10.1146/annurev.fluid.36.050802.122103`.

[40] A. A. Townsend. In *The Structure of Turbulent Shear Flow*. Cambridge University Press, 1976.

[41] A. Doosttalab, G. Araya, J. Newman, R. J. Adrian, K. Jansen, and L. Castillo. Effect of small roughness elements on thermal statistics of a turbulent boundary layer at moderate Reynolds number. *J. Fluid Mech.*, 787:84–115, 1 2016. ISSN 1469-7645. doi:10.1017/jfm.2015.676. URL `http://journals.cambridge.org/article_S002211201500676X`.

[42] H. Bocanegra Evans, S. Gorumlu, B. Aksak, L. Castillo, and J. Sheng. Holographic microscopy and microfluidics platform for measuring wall stress and 3d flow over surfaces textured by micro-pillars. *Sci. Rep.*, 6, 2016. doi:10.1038/srep28753. URL `http://dx.doi.org/10.1038/srep28753`.

[43]R. L. Simpson, J. H. Strickland, and P. W. Barr. Features of a separating turbulent boundary layer in the vicinity of separation. *J. Fluid Mech.*, 79(03):553–594, 1977.

[44]R. L. Simpson, Y.-T. Chew, and B. G. Shivaprasad. The structure of a separating turbulent boundary layer. part 1. mean flow and Reynolds stresses. *J. Fluid Mech.*, 113:23–51, 1981.

[45]A. E. Alving and H. H. Fernholz. Turbulence measurements around a mild separation bubble and downstream of reattachment. *J. Fluid Mech.*, 322(1):297–328, 1996.

[46]L. Sirovich. Turbulence and the dynamics of coherent structures. I - Coherent structures. *Q. J. Math.*, 45:561–571, October 1987.